Microfluid Nanofluid (2011) 11:269–282
DOI 10.1007/s10404-011-0794-5

RESEARCH PAPER

Equilibrium molecular dynamics studies on nanoscale-confined fluids

Murat Barisik · Ali Beskok

Received: 26 January 2011 / Accepted: 18 March 2011 / Published online: 3 April 2011

Abstract Fluid behavior within nanoscale confinements is studied for argon in dilute gas, dense gas, and liquid states. Molecular dynamics simulations are used to resolve the density and stress variations within the static fluid. Normal stress calculations are based on the Irving–Kirkwood method, which divides the stress tensor into its kinetic and virial parts. The kinetic component recovers pressure based on the ideal-gas law. The particle–particle virial increases with increased density, whereas the surface–particle virial develops because of the surface-force field effects. Normal stresses within nanoscale confinements show anisotropy primarily induced by the surface-force field and local variations in the fluid density near the surfaces. For dilute and dense gas cases, surface-force field that extends typically 1 nm from each wall induces anisotropic normal stress. For liquid case, this effect is further amplified by the density fluctuations that extend beyond the force field penetration region. Outside the wall-force field penetration and density fluctuation regions, the normal stress becomes isotropic and recovers the thermodynamic pressure, provided that sufficiently large force cut-off distances are used in the computations.

Keywords Wall-force field · Pressure · Normal stresses · Surface and particle virial

M. Barisik · A. Beskok (✉)
Institute of Micro and Nanotechnology, Old Dominion University, Norfolk, VA 23529-0247, USA
e-mail: abeskok@odu.edu

1 Introduction

Understanding the behavior of fluids and their manipulation within nanoscale confinements is of great interest for a vast number of applications that include the design of micro/nano electromechanical systems, microfluidic device components, and computer hard drives. Fluids inside the nanoscale channels can exhibit substantially different physics from what is observed in larger-scale systems because of the breakdown of the continuum hypothesis as well as the increased influence of the wall-force field effects. Deviations from the continuum behavior have been systematically studied for gas flows in the slip, transition, and free molecular flow regimes using the kinetic theory (Karniadakis et al. 2005). Most of these studies model the gas/surface interactions using simple reflection laws or scattering kernels with increased levels of sophistication (Karniadakis et al. 2005; Cercignani and Lampis 1971; Cercignani and Pagani 1966). However, these models do not directly account for the wall-force field effects, and they are not applied within a deterministic computational process, such as the molecular dynamics (MD) method. Although the wall-force fields are effective within a couple molecular diameters distance from the surface, such length scales are comparable to the dimensions of nanoscale channels and confinements, and thus their effects cannot be neglected. In fact, liquid transport in nanochannels has been studied extensively using MD, by using the appropriate wall/liquid interaction potentials (Li et al. 2010; Thompson and Troian 1997; Cieplak et al. 2001; Cieplak et al. 1999). Although these studies report density layering because of the wall-force field effects, comprehensive investigations of stresses induced on the nanoscale-confined liquids because of the surrounding surfaces are rather limited.

The wall-force field can induce adsorption of gas, liquid, or dissolved solids onto a surface (Toth 2002). For the most simplistic case, van der Waals forces between the fluid and solid molecules can induce significant changes on the fluid properties near a surface (Zhou 2007; Lee and Aluru 2010). Using the particle–surface interactions, adsorption theory focuses on the number of molecules adsorbed by a surface. Adhesion of gas or liquid molecules onto the surface creates a film of the adsorbate that is mostly immobilized on the adsorbent surface. Adsorption is a function of the solid–fluid interactions. The number of adsorbed molecules onto a surface can be theoretically calculated using intermolecular potentials between each adsorbent–adsorbate pair at a given temperature. Although useful, adsorption theory essentially uses "one-dimensional" force field based on the separation distance between the fluid–solid molecular pair and molecular structure of the surface (Steele 1973). As a result, the anisotropy in fluid density (i.e., density layering for liquids) and the corresponding stress distribution near a surface cannot be predicted accurately.

Investigation of the behavior of a fluid next to a solid surface requires careful considerations of wall-force fields. As the gradient of scalar potentials, the interatomic forces play a key role in the local stress tensor calculations. Different than an ideal-gas system of noninteracting point masses, these forces have significant contribution to the stresses in the near-wall regions, where the wall-force penetration depth extends a couple of molecular diameters from the surface and covers nonnegligible portions of a nanoscale domain. Consequently, stresses induced by the surface forces, identified as the "surface virial," should not be neglected (Tsai 1971).

The main *goal* of this study is to investigate the fluid density and normal stresses in the bulk and near-wall regions of simple fluids confined within nanoscale channels. MD simulations are conducted for argon at various fluid densities corresponding to the dilute gas, dense gas, and liquid states. Specifically, the surface virial effects are investigated at various fluid/wall potential strength ratios. To our knowledge, this work presents the density and normal stress distributions for a nanochannel-confined gas for the first time in literature. Liquid argon results exhibit well-known density layering and show normal stress variations in liquids, including the surface virial effects. Findings of this research clearly indicate the importance of the wall-force field effects in nanoscale confinements, which are mostly neglected in previous gas flow studies.

This article is organized as follows: In Sect. 2, we describe the MD simulation parameters. In Sect. 3, we explain the stress tensor computations and methods used in the MD algorithm. In Sect. 4, we present the dilute gas, dense gas, and liquid results. Normal stress components of the stress tensor are investigated by considering the contributions of kinetic and virial additive parts separately. Further discussions of the virial component and the relative importance of the particle–particle virial and the surface–particle virial terms are presented. Finally, we present the conclusions of our study.

2 Three-dimensional MD simulation details

We performed argon simulations confined between two infinite plates that are $H = 5.4$ nm apart by using the microcanonical ensemble (*NVE*) (i.e., constant mole, *N*, volume, *V*, and energy, *E*). We used the *truncated* (6–12) Lennard–Jones (L–J) potential to model the van der Waals interactions given as

$$V_{\text{truncated}}(r_{ij}) = 4\varepsilon\left(\left(\left(\frac{\sigma}{r_{ij}}\right)^{12} - \left(\frac{\sigma}{r_{ij}}\right)^{6}\right) - \left(\left(\frac{\sigma}{r_c}\right)^{12} - \left(\frac{\sigma}{r_c}\right)^{6}\right)\right), \quad (1)$$

where r_{ij} is the intermolecular distance, ε is the depth of the potential well, σ is the molecular diameter, and r_c is the cut-off radius. The mass for an argon molecule is $m = 6.63 \times 10^{-26}$ kg, its molecular diameter is $\sigma = 0.3405$ nm, and the depth of the potential well for argon is $\varepsilon = 119.8 \times k_b$, where k_b is the Boltzmann constant (1.3806×10^{-23} J K^{-1}). Simulations consider different states of argon as dilute gas, dense gas, and liquid states. The domain size, temperature, density, and other simulation details can be found in Tables 1 and 2.

Formally, all interactions between the nonbonded particles have to be calculated in MD. Because the L–J potential vanishes at larger molecular distances, only the interactions with particles within a certain cut-off radius (r_c) need to be calculated. Therefore, the intermolecular interaction forces were truncated and switched to zero at a certain cut-off distance. For L–J potentials, it is *customary* to use a cut-off distance of 1.08 nm, which is approximately equal to 3σ (Allen and Tildesley 1989). Using a larger cut-off distance does not affect the density predictions for L–J fluids. However, long-range attractive L–J interactions are crucial for accurate calculations of dense gas and liquid pressure. In this work, we employed various cut-off distances between the fluid molecules and compared our MD results with the corresponding thermodynamic state properties of argon to validate our findings (see Table 2). To model the wall effects consistently, we used a constant cut-off distance of 1.08 nm for fluid–surface interactions. Our algorithm uses the well-known link cell method to handle the particle–particle interactions (Allen and Tildesley 1989). Increasing the cut-off distance by a factor of *M* increases the computational load by M^6,

Table 1 MD simulation properties

State	Domain (nm)	T (K)	# Molecs.	ρ (#/nm^3)	ρ (#σ^3/nm^3)	ρ (kg/m^3)
Dilute gas	54 × 5.4 × 54	298	450	0.0286	0.0011	1.896
Dense gas	2.7 × 5.4 × 2.7	180	352	8.94	0.353	593.16
Compressed liquid	2.7 × 5.4 × 2.7	125	801	20.35	0.803	1349.8

Table 2 Simulation properties for the periodic cases, and comparison of pressure predictions with the thermodynamic state using various L–J force cut-off distances (r_c)

State	r_c (nm)	ρ^{-1} (m^3/kg)	T (K)	P_{table} (kPa)	P_{MD} (kPa)	Error (%)	$P_{\text{ideal gas}}$ (kPa)	Z_{table}
Dense gas	1.08	0.00505	298.2	11,680	11,831	1.30	12,288	0.95
Dense gas	2.7	0.00505	298.2	11,670	11,705	0.30	12,288	0.95
Dense gas	1.08	0.00505	179.5	5,519	5,743	4.06	7,397	0.75
Dense gas	2.7	0.00505	178.2	5,451	5,483	0.58	7,345	0.74
Dense gas	1.08	0.002525	180.3	8,771	8,971	2.28	14,861	0.58
Dense gas	2.7	0.002525	181.9	8,699	8,726	0.31	14,992	0.58
Dense gas	1.08	0.001687	183.3	12,290	13,723	11.66	22,547	0.55
Dense gas	2.7	0.001686	178.9	10,820	11,157	3.11	22,092	0.49
Dense gas	1.08	0.001318	162.1	9,145	11,384	24.48	25,425	0.36
Dense gas	2.7	0.001319	166.2	10,630	9,797	−7.83	26,233	0.41
Compressed liquid	1.08	0.000741	125.4	52,670	68,677	30.39	–	–
Compressed liquid	2.16	0.000741	127.7	56,310	59,707	6.03	–	–

because the computational cost for MD is proportional to the square of the number of molecules contained within a cell.

Gas states evolve through intermolecular collisions separated by ballistic motion of particles characterized by the "mean free path (λ)." To allow intermolecular collisions, gas simulation domains should be on the order of λ in the lateral and axial directions. This requirement results in relatively large simulation volumes for classical MD, which necessitates modeling of a large number of gas molecules and excessively large number of wall molecules. To address this computational difficulty, we used the recently developed "smart wall" MD (SWMD) algorithm (Barisik et al. 2010). For L–J molecules interacting with FCC (face centered cubic) wall structures ((1,0,0) plane facing the fluid), the SWMD uses 74-wall molecules as a stencil for fluid–surface interactions. Because of the cut-off distance of the L–J potentials, such a small stencil of wall molecules properly incorporates the wall-force field effects of an infinite wall; significantly reducing the memory requirements for MD simulations (Barisik et al. 2010). For simplicity, the FCC-structured walls have the same molecular mass and molecular diameter of argon ($\sigma_{\text{wall}} = \sigma_{\text{argon}}$). Periodic boundary conditions are applied in the axial (x) and lateral (z) directions. Overall, the computational domain size is related with the mean free path of the gas states. As a result, domain sizes of ($\lambda \times H \times \lambda$) 54 × 5.4 × 54 nm, 2.7 × 5.4 × 2.7 nm, and 2.7 × 5.4 × 2.7 nm are selected for dilute gas, dense gas, and liquid cases, respectively. Based on our previous work, one mean free-path long-domain sizes in the periodic dimensions are sufficient to obtain MD solutions for gas flows, independent of the periodicity effects (Barisik et al. 2010).

Simulations started from the Maxwell–Boltzmann velocity distribution at corresponding simulation temperatures given in Tables 1 and 2. Initial particle distribution is evolved 10^6 time steps (4 ns) to reach an isothermal steady state using 4 fs ($\sim 0.002\tau$) time steps using a thermostat. This initial procedure ensures that the fluid system attains equilibrium in presence of the surfaces at desired temperatures. After which, 2×10^6 time steps (8 ns) are performed for time averaging in a thermostat free domain. Longer time averaging has also been performed to confirm convergence of the density and stress profiles to the steady state. Particularly, the simulation times are compared with the mean collision times (predicted by the ratio of the mean free path to the mean thermal speed $c_m = \sqrt{8RT/\pi}$) to result in a state amenable for time or ensemble averaging. The computational domain is divided into 100 bins of approximately $\sigma/10$ in size to resolve the near-boundary region accurately.

Two different thermostat techniques are also employed to study their effects in the case of nonequilibrium MD simulations. The Nose–Hoover thermostat is applied to the

fluid molecules at each time step to obtain isothermal condition with a fixed lattice model (Evans and Hoover 1986). This deterministic algorithm achieves temperature control by extended system dynamics. In addition, a recently developed thermally interacting wall model is used to simulate the flow domain free of thermostat effects (Kim et al. 2008a), which allows specification of a constant wall temperature induced by a velocity-scaling thermostat. In this method, the walls have their own thermal oscillations, and they exchange momentum and energy with the fluid particles through intermolecular interactions. This approach enables simulation of heat transfer between the fluid and a surface, and properly dissipates heat through the thermostat applied on the walls (Kim et al. 2008a, b, 2010).

3 Computation of the stress tensor components

Computations of the stress tensor components for an atomistic system have two additive components. The first is kinetic contribution from throughput of linear momentum resulting from the particle velocities, whereas the second components is the virial term, which is an internal contribution from intermolecular forces between the particles. In our simulations, Irving–Kirkwood expression was used to compute the stress tensor components for an N particle system as follows (Irving and Kirkwood 1950):

$$S_{kl} = \frac{1}{\mathrm{Vol}} \left\langle \sum_{i}^{N} m^i (V_k^i - \overline{V}_k^i)(V_l^i - \overline{V}_l^i) + W_{kl} \right\rangle, \tag{2}$$

$$W_{kl} = \frac{1}{2} \sum_{i,j}^{N} (r_k^j - r_k^i) f_l^{i,j}, \tag{3}$$

where the first term on the right-hand side of Eq. 2 is the kinetic and the W_{kl} term is the virial component. In the kinetic part, m^i is the atomic mass of particle i, whereas k and l are the axes of the Cartesian coordinate system, V_k^i and V_l^i are the peculiar velocity components of particle i in the k and l directions, and $\overline{V}_k^i$ and $\overline{V}_l^i$ are the local average streaming velocities at the position of particle i, in the k and l directions, respectively. For nonequilibrium systems, the local streaming velocities should be subtracted from the equilibrium velocities to establish mechanical equilibrium at the system's center of mass. For the virial component, $\left(r_k^j - r_k^i\right)$ in Eq. 3 is kth component of the relative distance vector between particles i and j, and $f_l^{i,j}$ is the lth component of the intermolecular force exerted on particle i by particle j.

The first term in the Irving–Kirkwood expression is related to the ideal-gas law. For an ideal gas in equilibrium (i.e., zero peculiar velocity and no virial), the average normal stress because of the kinetic terms results in

$$\frac{S_{xx} + S_{yy} + S_{zz}}{3} = \frac{1}{3\mathrm{Vol}} \left\langle \sum_{i}^{N} m^i (V_k^i)^2 \right\rangle = \frac{NkT}{\mathrm{Vol}} = P. \tag{4}$$

Therefore, kinetic part of the Irving–Kirkwood expression calculates ideal-gas pressure exactly by considering the momentum resulting from the particle velocities, whereas the particle–particle virial terms are corrections to the ideal-gas law because of the interaction of particles having non-zero volumes and force fields. Accurate prediction of pressure, and hence, the thermodynamic state for dense gas and liquids requires considering of the long-range force field interactions between the particles, where the particle–particle virial calculations in Eq. 3 have significant effects. Specifically, the L–J force between a molecule pair experiences sign change at a distance of $2^{1/6}\sigma$ which corresponds to 0.3822 nm for argon molecules. For regions where the mean molecular spacing is lower than 0.3822 nm, the intermolecular forces are repulsive and the virial terms are positive. For larger mean molecular spacing, the intermolecular forces are attractive and the virial terms become negative. Therefore, local fluid density and the resulting mean molecular spacing carry an important role in the sign of the particle–particle virial terms.

Use of the *NVE* ensemble fixes the fluid density and energy. Because there is no flow or heat flux in the system, fixed energy simulations result in constant temperature. Therefore, one can obtain the correct density and temperature distributions in the domain, while the pressure calculations are sensitive to the long-range intermolecular force interactions. Simply increasing the cut-off distance of the L–J force interactions intensifies the computational cost tremendously. Having recognized this deficiency, *empirical* corrections to the MD-based pressure calculations using the Irving–Kirkwood expression have been proposed to model the long-range force interactions (Frenkel and Smit 2002). Because the objective of our study is the investigation of the wall-force field effects in nanoscale-confined fluids, we paid specific attention to accurate calculations of the local pressure. A detailed discussion on the prediction of local thermodynamic state for dense gas and liquid argon is presented in the Sect. 4 as a function of the MD cut-off distance used in computations. As can be seen in Table 2, the absolute error in MD prediction of local pressure at a given thermodynamic state is less than 8%.

In the following section, we use Eqs. 2 and 3 for nanoscale-confined dilute gas, dense gas, and liquid systems and calculate the normal stress components across nanochannels. We will distinguish the virial effects given in Eq. 3 because of the particle–particle and surface–particle interactions. Before we proceed further, we must indicate that the off-diagonal components of the stress tensor (i.e., shear stresses) were also computed. Shear

stresses on the fluid induced by the stationary walls were zero, as expected. Given this fact, the normal stress components and their directions presented in this study correspond to the principle stresses and directions for fluids confined in stationary nanochannels.

4 Results

4.1 Dilute gas

We first focus on argon at 298 K and 1.896 kg/m^3 (see Table 3 for computed and ideal-gas pressure values). This state corresponds to dilute gas, because the mean molecular spacing to molecular diameter ratio is 9.6. Mean free path of argon at this state is 54 nm. MD simulations are performed in a nanochannel of 5.4 nm in height and 54 nm in length and width. The simulation contains 450 argon molecules. The resulting number density is 0.0286 #/nm^3. Systematic studies are performed for various argon–wall interaction strengths by varying the $\varepsilon_{\text{wall-Ar}}/\varepsilon_{\text{Ar–Ar}}$ ratio (= ε_{wf}). A snapshot of the computational domain is shown in Fig. 1a for $\varepsilon_{\text{wf}} = 1$ case, where periodic boundary conditions are imposed along the channel length and width. As can be seen from the figure, the SWMD introduces a stencil of wall molecules on the surface when a fluid molecule approaches to the surface within the cut-off distance of the L–J potential (1.08 nm used for dilute gas cases). Therefore, wall stencils in the figure show the locations where argon molecules are in the vicinity of the surface. Comparison of the mean free path to the channel height results in the Knudsen number (*Kn*) of 10. In the case of flow, driven by a pressure gradient, force field, or the motion of surfaces, argon gas would have been in the free molecular flow regime, where gas–wall interactions overwhelm the gas–gas collisions (Karniadakis et al. 2005). Although the flow cases are out of scope of the current study, density and normal stress distributions for nanochannel-confined fluid are precursor for future flow studies.

Figure 2a shows the density variation within half of the nanochannel for $\varepsilon_{\text{wf}} = 1$ case, obtained using the Nose–Hoover thermostat, interactive thermal wall model, and without using a thermostat. The latter case is based on the microcanonical ensemble (*NVE*), which is appropriate here, because no external work is done on the system. The Nose–Hoover and interactive thermal wall model use NVT ensemble on the fluid and surfaces, respectively. Identical density distribution within the nanochannel is predicted using all three methodologies. A density buildup near the surface is observed. For $\varepsilon_{\text{wf}} = 1$, gas density near the surface increases almost three times with a single peak point, representing accumulation near the surface. This behavior is because of the surface potentials increasing the residence time of particles inside the force penetration depth. Molecules are not immobilized on the surface. Instead, they are trapped in the wall potential field for a certain time period and experience multiple collisions with the surface. Because the simulation domains are in equilibrium, some of the trapped particles can leave and resume their free flights, while new particles get inside the force penetration region. Therefore, the density is a constant both in the bulk and near-wall regions. The density particularly starts to deviate from its bulk value around 2.5σ from the wall. We must indicate that accumulation near the boundary results in slight reductions in gas density in the bulk of the channel. Specifically, the bulk density reduces to 0.0275 #/nm^3 or 96% of its assigned value. This density reduction is because of the constant number of gas molecules (*N*) used in MD simulations. Because the gas molecules cannot penetrate to the bins neighboring the wall, gas density goes to zero on the wall. Figure 2b shows the temperature profile in the nanochannel obtained without a thermostat. The Nose–Hoover thermostat and interactive thermal wall model techniques predict the same temperature in the system (not shown). Gas is essentially under isothermal conditions at 298 K. Near-wall gas temperature approaches zero because of zero gas density near the walls.

Density variations within the nanochannel are induced by the wall-force field. It is important to investigate the effects of these force fields within the perspective of normal stresses, which can be eventually related to pressure within this simple compressible system. Figure 3 shows the distribution of three mutually orthogonal components of normal stresses within the nanochannel. As stated earlier, the off-diagonal terms of the stress tensor are zero. Therefore, these normal stresses correspond to the principle stresses, and they are acting in three mutually orthogonal directions that coincide with the directions of the Cartesian coordinate system used in this study. Specifically, the channel length and width are in *x*- and *z*-directions,

Table 3 Comparison of MD calculated pressure values with the thermodynamic state in nanoscale confinements

State	r_c (nm)	ρ^{-1} (m^3/kg)	T (K)	P_{table} (kPa)	P_{MD} (kPa)	Error (%)	$P_{\text{ideal gas}}$ (kPa)	Z_{table}
Dilute gas	1.08	0.5494	298	113	113	0	113	1
Dense gas	2.7	0.00168	180.2	11,620	10,926	−5.98	22,166	0.52
Compressed liquid	2.7	0.0007065	124.8	80,840	86,000	6.4	–	–

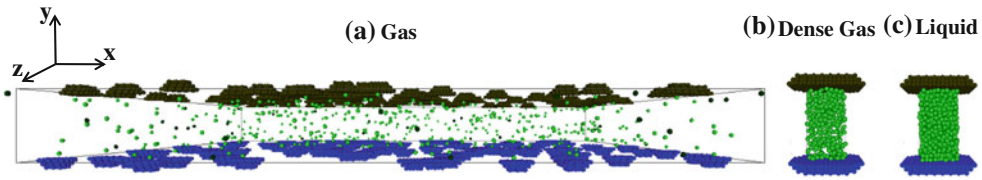

Fig. 1 Snapshots of dilute gas (**a**), dense gas (**b**), and liquid (**c**) simulation domains

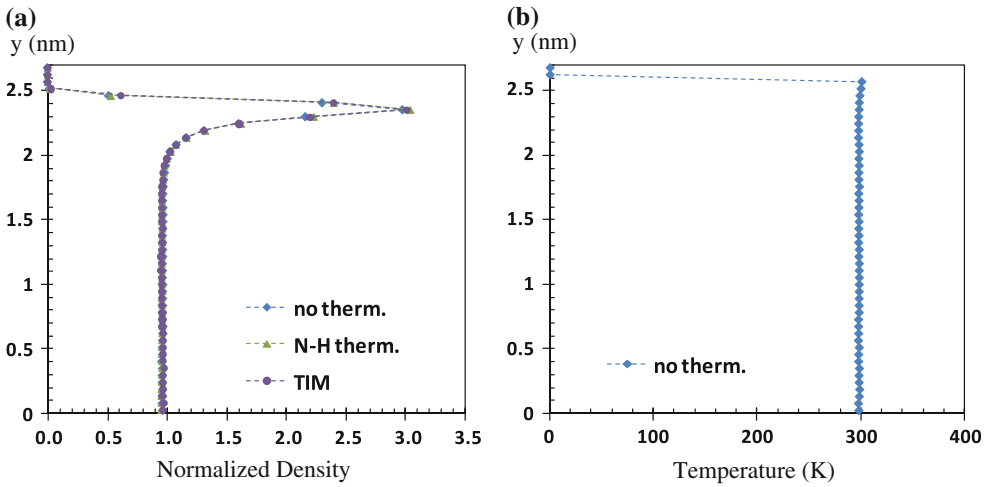

Fig. 2 **a** Normalized density distribution of the dilute gas case obtained using different thermostat techniques (*N–H therm* Nose–Hoover thermostat, *TIM* thermally interacting wall). Simulations were performed for average density of 0.0286 #/nm^3. Results for $\varepsilon_{wf} = 1$ are shown. **b** Temperature distribution verifies isothermal conditions at 298 K

whereas the channel height is in y-direction. Therefore, S_{xx}, S_{yy}, and S_{zz} are the normal stresses at a point that act in the x-, y-, and z-directions, respectively. We have used Eq. 2 to calculate the stresses. Particularly, we distinguish between the kinetic and virial parts of Eq. 2, which are shown in Figs. 3a and b, respectively, whereas Fig. 3c shows the total normal stresses as the sum of the kinetic and virial components. The virial term is often dominant for liquids, whereas the kinetic term is more dominant for gas flows, as suggested by Irving and Kirkwood (1950). Our calculations have shown that the contribution of the virial component in the bulk region (i.e., outside the wall-force field cut-off distance, which is approximately $y \leq 1.7$ nm in the figures) is less than 0.05% of the resulting normal stress. In fact, the normal stresses because of the kinetic terms in Eq. 2 are isotropic in the entire channel, and variation of the kinetic part of the normal stresses shown in Fig. 3a is similar to the density variations shown in Fig. 2a under isothermal conditions. In the bulk portion of the channel ($y \leq 1.7$ nm), pressure can be calculated as the average of the following three normal stress components

$$P = \frac{S_{xx} + S_{yy} + S_{zz}}{3}.$$

The pressure field predicted using the computed density and temperature within the ideal-gas law matches the computed pressure distribution exactly. This is an expected behavior, as explained earlier in Sect. 3.

Virial terms in the bulk region are isotropic, and their contribution to pressure is negligible. However, this is not the case in the near-wall region, as can be seen from Fig. 3b, where the surface virial effects induce anisotropy and significant deviations from the ideal-gas behavior in the near-wall region. Different than the bulk portion, virial term dominates the normal stress distribution inside the force penetration depth. Behavior of the virial terms is rather sensitive to the net force field and local density changes, and affected by the particle–particle and particle–wall interactions. The virial terms in x- and z-directions are identical, whereas the virial in y-direction (i.e., normal to the wall) shows significant deviations from the previous two components.

Figure 4 shows the variations of the yy component of the particle–particle (a) and surface–particle (b) virial terms in y-direction. In the bulk flow region, the particle–particle virial results in weak attractive forces (shown by the negative-stress values in Fig. 4a). However, increase in the gas density near the wall induces local repulsive forces, increasing the particle–particle virial rapidly as a result of the surrounding gas molecules. As the local gas density reaches a peak and starts to decline, the particle–particle virial term starts to decrease. The surface virial in y-direction is shown in Fig. 4b. Although its value is zero in the bulk region, the surface virial becomes dominant in the near-wall region, overwhelming both the particle–particle virial and kinetic terms. The surface virial variation

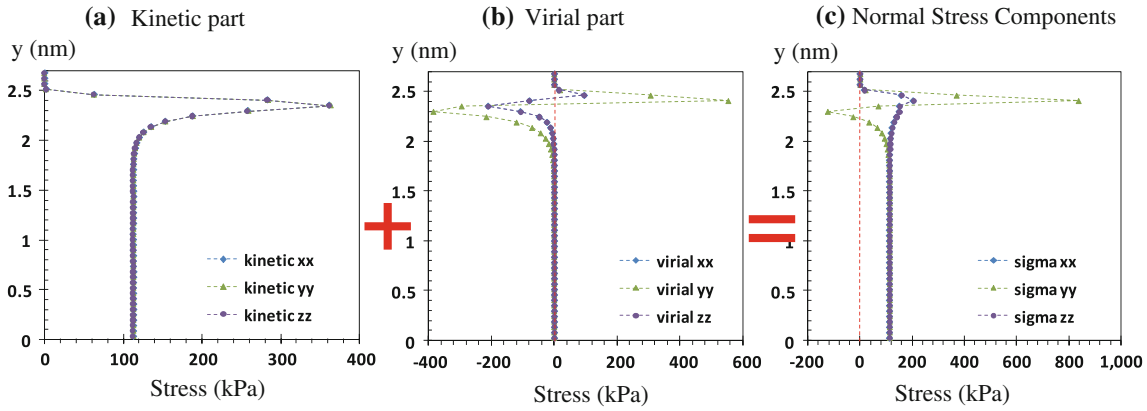

Fig. 3 Kinetic (**a**) and virial (**b**) components of the normal stress distribution (**c**) for the dilute gas case

is nonmonotonic. To understand its behavior, we present in Fig. 5 the surface virial part of S_{yy} as a function of the distance from the wall. Figure 5 also includes the gas density variation within one nanometer from the wall and the potential and force fields induced by the *entire* FCC wall onto a single molecule approaching normally to the surface through the centerline of a wall molecule (represented in Fig. 5). The value of the surface virial is in kPa, and should be read from the left ordinate (axis *a*), whereas the gas density, wall potential, and force fields are normalized by the values stated in the caption of Fig. 5, and their values should be read from the right ordinate (axis *b*) in nondimensional form. Keeping in mind that the potential and force fields in the Fig. 5 are the result of the *entire wall structure*, we first discuss the density distribution near the surface, which exhibits its peak value at the potential minimum. After this minimum, the potential increases exponentially and hence, the density profile converges to zero. One may expect observing infinite potential and zero density one molecular diameter distance from the wall by simply considering the L–J potential. However, the molecular corrugations because of the structure of FCC walls allow some gas molecules penetrate into the one molecular diameter region, resulting in gradual convergence of density distribution to zero.

As the gradient of a scalar potential, the force field in normal direction to the wall is also plotted in Fig. 5. The normal force reaches zero at the potential minimum, as indicated by the vertical dashed line at $y \approx 0.36$ nm. The negative- and positive-force values show attractive and repulsive behaviors, respectively. The surface virial in *y*-direction is negative through the attractive portion of the wall potential. The surface virial decreases up to the zero-force point after which it becomes repulsive and starts increasing rapidly toward the wall. However, this increase is limited and finally overwhelmed by the decrease in the density of gas molecules near the surface. As a result, the surface virial terms decrease and converge to zero. Overall, the variation in surface virial is a function of the wall-force field as well as the local gas density. We investigated the surface virial behavior for different gas/wall interaction strength ratios (ε_{wf}), which has shown similar behavior to the results depicted in Fig. 5 with an approximately linear increase in the magnitude of the virial terms with increased ε_{wf} ratio (results are not shown for brevity).

The number of argon molecules in the channel under various gas/wall interaction strength ratios (ε_{wf}) is shown in Fig. 6. The near-wall gas density increases with increasing the gas/wall interaction strength ratio, which leads to gradual decrease of the number of gas molecules in the bulk region. An increased residence time for gas molecules within the force penetration region is observed. For the $\varepsilon_{wf} = 3$ case, more than 360 of 450 molecules are mostly like to spend time in the near-wall region at a given instant. However, identity of these gas molecules can still change by time. Therefore, some molecules are able to leave the surface-force field and continue their free flight toward the opposing surface. Further increase of the wall strength results in adsorption of argon on the surfaces with bulk region being depleted from gas molecules.

Variations of the *xx* and *yy* components of normal stresses in the nanochannels are shown in Fig. 7 for different gas/wall interaction strength ratio (ε_{wf}) values. The stress profiles are normalized using the channel center pressure values of 126.1, 113, and 83.9 kPa for the $\varepsilon_{wf} = 0.4$, 1.0, and 1.8 cases, respectively. Kinetic parts of stress profiles are proportional to the density distributions, and match ideal-gas predictions in the bulk region. Increase in the ε_{wf} results in stronger surface–particle interactions, and hence, the surface virial becomes more dominant. Figure 7b illustrates the *yy*-component of normal stress for different ε_{wf} values. Trends in 7b are similar for all ε_{wf} cases. However, the magnitude of the stress increases with increased ε_{wf}. Surface–particle virial is dominant within the wall-force field penetration depth, initially inducing an attractive force (negative-stress values) followed by strong

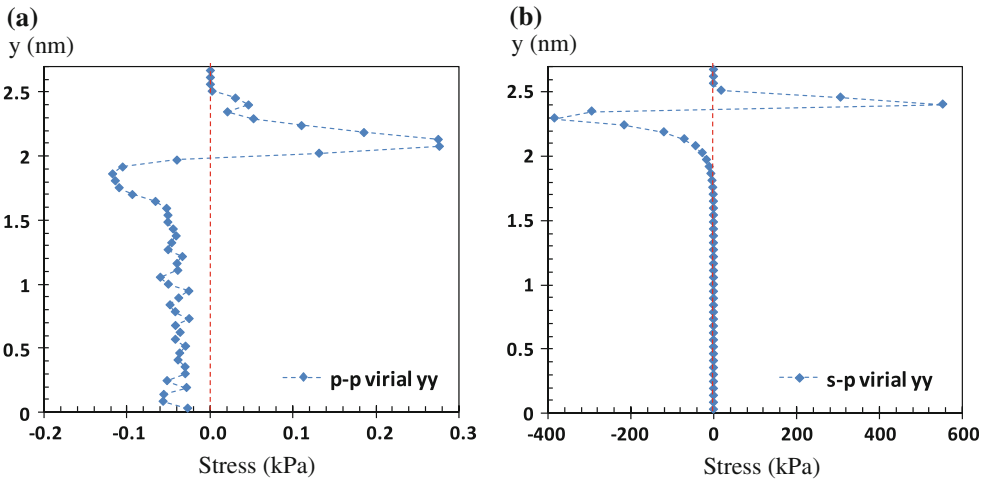

Fig. 4 Variation of the *yy* component of the particle–particle (**a**) and surface–particle (**b**) virial terms within half of the nanochannel for the dilute gas case

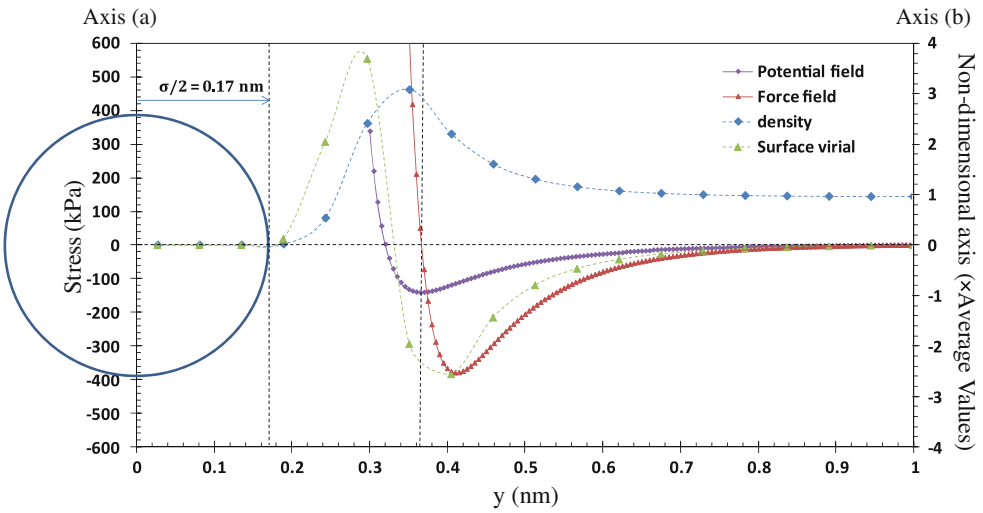

Fig. 5 Spatial variation of the surface virial (*left ordinate*), gas density, wall potential, and force fields (*right ordinate*) in the near wall region. The density, potential, and force terms are normalized by 0.0286 #/nm^3, -0.205×10^{-20} kg m^2/s^2, and 2.034×10^{-20} N, respectively. The potential and force fields induced by the entire FCC wall onto a single molecule approaching normally to the surface through the centerline of a wall molecule is shown. A representation of the wall molecule is also included

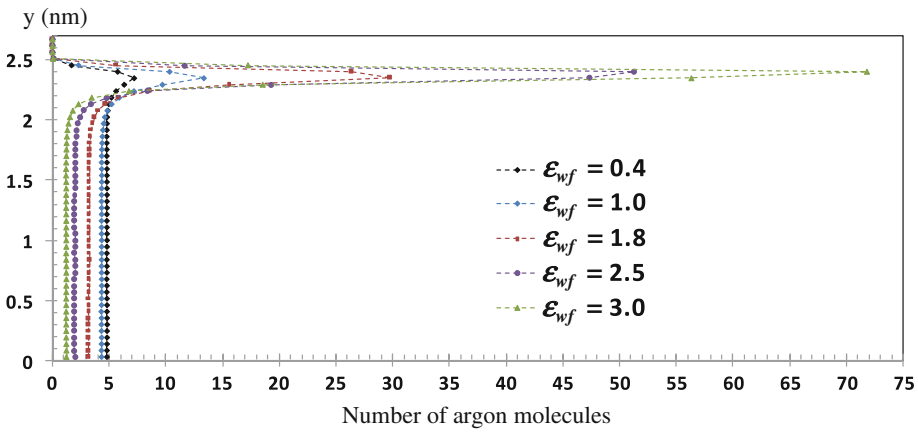

Fig. 6 Number of argon molecules across the nanochannel obtained for different gas/wall interaction strength ratios (ε_{wf})

repulsion (positive-stress values). In Fig. 7a, sudden variations in the *xx*-component of normal stresses for the $\varepsilon_{wf} = 1.8$ case are because of the negative surface–particle virial becoming more dominant than the positive kinetic component. Local variations of the kinetic and virial components of these stresses are not shown for brevity.

4.2 Dense gas

To predict the correct thermodynamic state of dense argon gas, we performed a series of dense gas simulations in periodic domains spanning $\lambda \times \lambda \times \lambda$, where λ is the local mean free path. We selected the density and temperature of

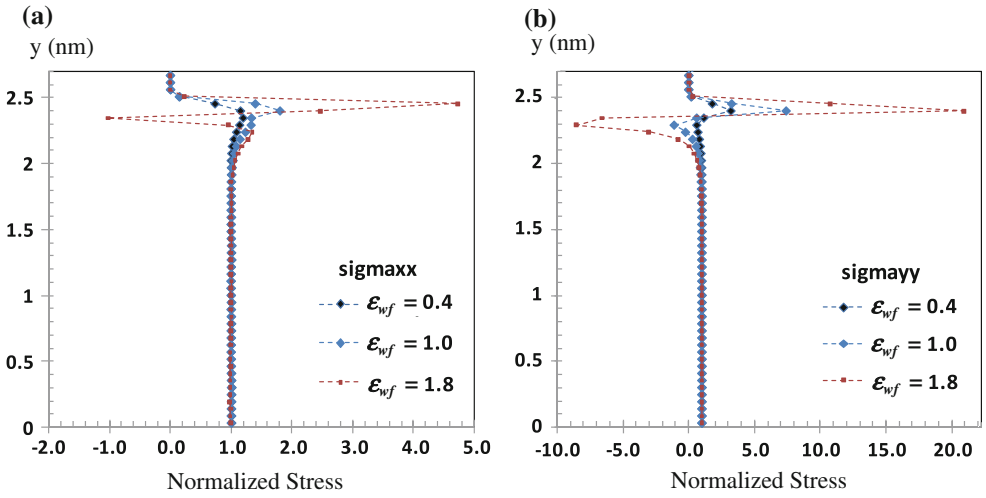

Fig. 7 Variations of the *xx* (**a**) and *yy* (**b**) components of the normal stress in the nanochannel for different gas/wall interaction strength ratios (ε_{wf}). The stresses are normalized using the bulk pressure values of 126.1, 113, and 83.9 kPa for the $\varepsilon_{wf} = 0.4$, 1.0, and 1.8 cases, respectively

argon gas at various states indentified in Table 2 and computed pressure using Eq. 2. We used different cut-off distances for intermolecular forces in pressure computations. Increasing the cut-off distance from 1.08 to 2.7 nm results in better agreements between the MD and pressure values tabulated in Sonntag and Borgnakke (2002). We also computed the compressibility factor Z (= $P/\rho RT$), which shows deviations from the ideal-gas law. Thus, $1 - Z$ shows relative importance of the particle–particle virial terms in Eq. 2. An example of a compressed liquid state of argon is also computed. Pressure of the liquid was successfully predicted using a cut-off distance of 2.16 nm. Using shorter cut-off distance in L–J interactions neglects weakly attractive forces between the molecules. As a result, the thermodynamic pressure is consistently over-predicted. Effects of using short cut-off distances in MD calculations were studied earlier in Mecke et al. (1997) and Guo and Lu (1997).

Dense argon gas is studied at 180 K and 593.16 kg/m^3 (number density of 8.94 #/nm^3) by simulating 352 argon molecules in a nanochannel of 5.4 nm in height and 2.7 nm in length and width (see Table 1). MD simulations are performed using the L–J force cut-off distance of 2.7 nm. Mean free path of argon at this state is 0.173 nm and the mean molecular spacing is 0.482 nm. The ratio of mean molecular spacing to molecular diameter is 1.42, which corresponds to a dense gas state. Local thermodynamic pressure is 11.62 MPa and the compressibility factor $Z = 0.52$ (see Table 3). Periodic boundary conditions are applied along the channel length and width. Figure 1b shows a snapshot of the computational domain for the $\varepsilon_{wf} = 1$ case.

Density distributions in the nanochannel obtained using the Nose–Hoover thermostat, interactive thermal wall model, and without using a thermostat are shown in Fig. 8. Density profile obtained using 1.08 nm force cut-off distance is also shown in Fig. 8. The near-surface gas density is larger than the bulk density. Unlike the dilute gas case with a single density peak, we now observe a dominant second density peak and a much weaker third density peak, indicating the onset of density-layering effects.

Figure 9c shows the distributions of the normal stress components along with their kinetic (Fig. 9a) and virial (Fig. 9b) contributions. We first examine the stress distribution in the bulk of the channel ($y \leq 1.5$ nm), where the surface–particle virial effects are zero. Away from the walls, the particle–particle virial contribution is −11.24 MPa. Negative sign of the normal stresses shows attractive forces on the molecules. At this state, the mean molecular spacing is 0.482 nm, where the L–J force interactions are attractive. The kinetic part of the normal stresses is isotropic and reaches 22.166 MPa in the bulk of the channel. Combination of the positive kinetic components of normal stresses with the negative particle–particle virial components results in local pressure of 10.926 MPa, a value 6% lower than the thermodynamic pressure of 11.620 MPa (Sonntag and Borgnakke 2002). Different than the bulk region, virial terms dominate the near-wall stress distribution with anisotropic behavior similar to that discussed for the dilute gas state. Non-monotonic variation of the surface–particle virial is similar to the dilute gas case shown earlier in Fig. 4. However, the minimum and maximum values of the surface–particle virial are now −100 to 80 MPa, respectively. Overall, the dense gas state acts as a transition between the dilute gas and liquid cases. Therefore, further discussions are given in the liquid results. Higher ε_{wf} cases, not shown for brevity of our discussions, resulted in higher surface virial magnitudes with almost linear increase in their magnitude.

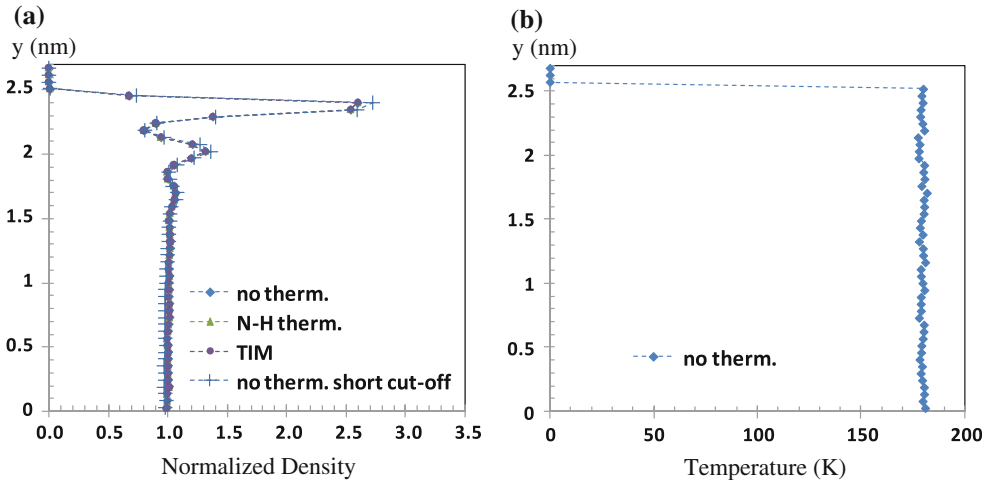

Fig. 8 Normalized density distribution of the dense gas case obtained using different thermostat techniques (**a**). Simulations were performed for average density of 8.94 #/nm^3. Results for $\varepsilon_{wf} = 1$ are shown. Temperature distribution verifies isothermal conditions at 180 K (**b**)

4.3 Liquid

Liquid argon at 125 K and 1,349.8 kg/m^3 is studied inside a nanochannel of 5.4 nm in height and 2.7 nm in length and width. Figure 1c illustrates a snapshot of the computational domain for the $\varepsilon_{wf} = 1$ case. Periodic boundary conditions are imposed along the channel length and width. The simulation contains 801 argon molecules with a resulting number density of 20.35 #/nm^3. The mean molecular spacing is 0.366 nm, which is comparable with the molecular diameter of argon.

Density distributions obtained using the Nose–Hoover thermostat, interactive thermal wall model, and without using a thermostat give identical results under isothermal conditions at 125 K (Fig. 10a and b). Density distributions obtained using 1.08 and 2.7 nm cut-off distances (r_c) for intermolecular force interactions are also shown in Fig. 10a. Density distribution is not affected by r_c. Similar to the previous researchers, multiple density layering is observed on the surface. In the direction normal to the interface, liquid density profiles exhibit oscillatory behavior on the *molecular scale* because of the interactions between the liquid and solid molecules. The magnitude of the density layering increases with increasing solid–liquid interaction strength ratio (ε_{wf}). Detailed investigation of density for different epsilon ratios can be found in Li et al. (2010), Thompson and Troian (1997), Cieplak et al. (2001), and Cieplak et al. (1999). Ordering of the liquid extends wall effects more into the bulk portion of the channel, compared with the gas cases. This dominant behavior at the solid–liquid interface has a major effect on the mechanical properties.

Stress tensor computations were performed using an L–J force cut-off distance of 1.08 and 2.7 nm. Kinetic components of the stresses (proportional to the density variation through the ideal-gas law) were unaffected from the use of the shorter cut-off distance. However, the virial contributions of the stress tensor were overestimated because of the negligence of the long-range weakly attractive interaction forces (results not show for brevity). In the following, we only show the results obtained using the cut-off distance of 2.7 nm.

Normal stress distribution in liquid argon interacting with walls at $\varepsilon_{wf} = 1$ is shown in Fig. 11c along with the

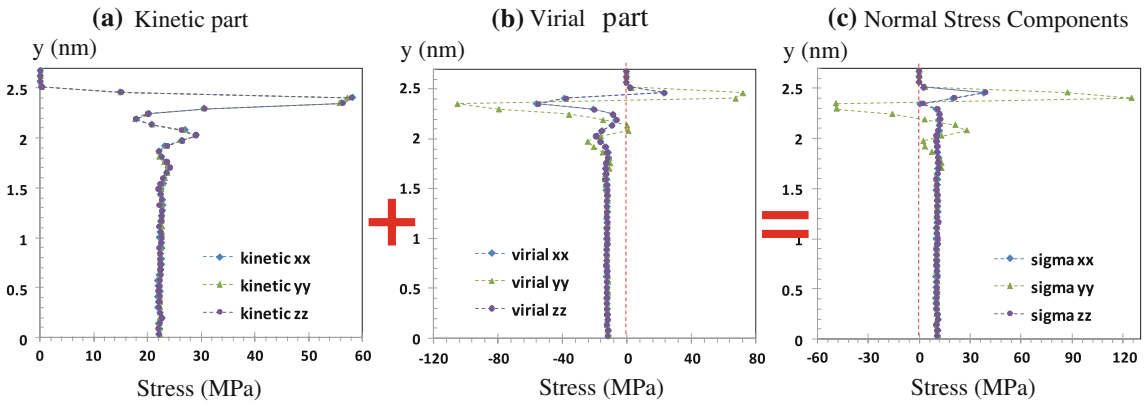

Fig. 9 Kinetic (**a**) and virial (**b**) components of the normal stress distribution (**c**) for the dense gas case

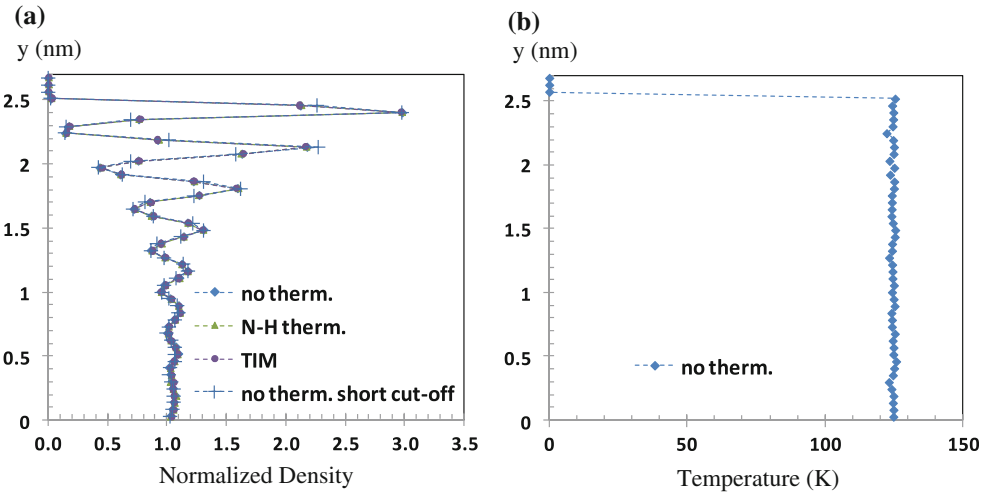

Fig. 10 Normalized density distribution of the liquid case with different thermostat techniques and using L–J force cut-off distances of $r_c = 1.08$ nm and 2.7 nm (**a**). Simulations were performed for average density of 20.35 #/nm^3. Temperature distribution verifies isothermal conditions at 125 K (**b**)

contributions of their kinetic (Fig. 11a) and virial (Fig. 11b) components. Oscillatory behavior of normal stresses arising from the density layering is apparent in the results. The normal stresses are anisotropic. Specifically, S_{yy} behaves differently than S_{xx} and S_{zz}. Similar to the gas cases, the stress tensor is diagonal. Therefore, the stresses shown in Fig. 11a–c correspond to the principle stresses on the liquid, and x-, y-, and z-directions correspond to the principle directions. A small isotropic region near the channel center is having constant and equal normal stresses (i.e., pressure) at 86 MPa; this region is bigger in a larger channel. The MD-calculated pressure is about 6.4% larger than the tabulated value of 80.84 MPa (see Table 3). It is worth mentioning that addition of a single molecule to this nanoscale system induces 0.125% variation in the liquid density, which increases the pressure by 1.34%. As expected from a compressed liquid state, small variations in the liquid density (at constant temperature) induce large changes in pressure; and discrete nature of the nanoscale system (i.e., limited volume and finite number of molecules) can induce large fluctuations in the calculated thermodynamic state. In the bulk region of the channel, the kinetic and virial contributions of pressure are the same order of magnitude. Specifically, the kinetic and virial components of stresses at the channel center are 37.54 and 48.46 MPa, respectively. The kinetic part of normal stresses is isotropic, and obeys the ideal-gas law. Because temperature is a constant, kinetic component of the normal stresses shows fluctuations similar to the fluid density. Virial part of the normal stresses is positive in the bulk of the channel, indicating repulsion between the molecules. The reason of this repulsive force is that the liquid argon molecules at this state are at a mean molecular spacing of 0.366 nm, where the intermolecular forces for the L–J potential are repulsive. As shown in Fig. 11b, the virial terms become dominant in the near-wall region and their behavior are sensitive to the net force field and local density changes. The virial in y-direction shows significant deviations from the x- and z-components. Different than the gas cases, anisotropic nature of normal stress distribution extends beyond the surface-force penetration depth of 3σ. The reason of this behavior is the density layering, which induces anisotropic normal stresses because of the particle–particle virial terms in Eq. 2.

Figure 12 shows the variations of the yy component of the particle–particle (Fig. 12a) and surface–particle (Fig. 12b) virial terms in y-direction. The particle–particle virial has strong influence of the density layering. It has oscillatory positive-stress values showing mostly strong repulsive forces in the bulk region. Decrease of the intermolecular distances inside the compact density layers of the near-wall region induces stronger local repulsive forces between the molecules that can be observed as increased positive-virial values. At density values smaller than the mean liquid density, the intermolecular spacing between the fluid layers is increased and the particle–particle interaction may become weakly attractive if the local molecular spacing increases beyond 0.3822 nm (i.e., the distance between two molecules, when the L–J force switches sign). These effects decrease the particle–particle virial. Figure 12b shows variation of the surface virial in y-direction. Surface virial effects overwhelm both the particle–particle virial and kinetic terms inside the force penetration depth before it converges to zero around the L–J cut-off distance.

Variations of the yy component of the surface–particle and particle–particle virial terms (Axis a) and the normalized density distribution (Axis b) inside a region 2 nm from the wall are shown in Fig. 13. Unlike the ideal-gas case, potential variation induced by the entire FCC wall onto a single molecule approaching normally to the surface

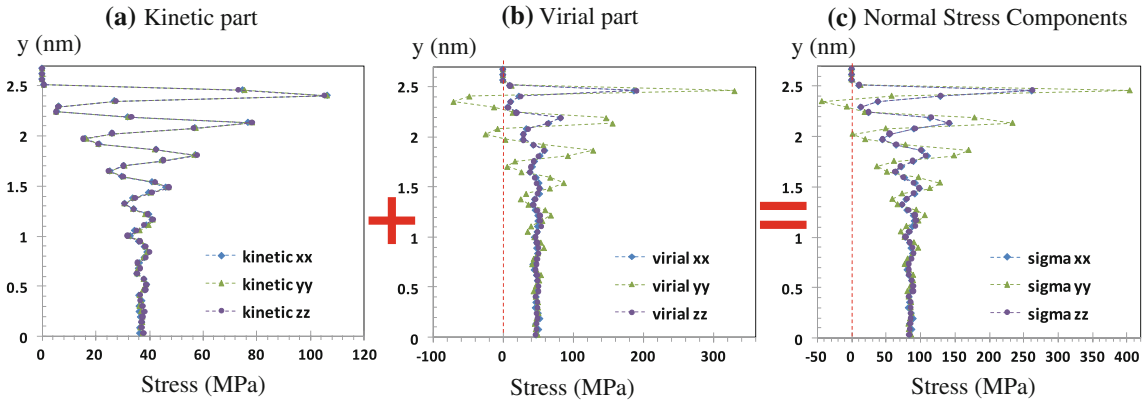

Fig. 11 Kinetic (**a**) and virial (**b**) components of the normal stress distribution (**c**) for the liquid case

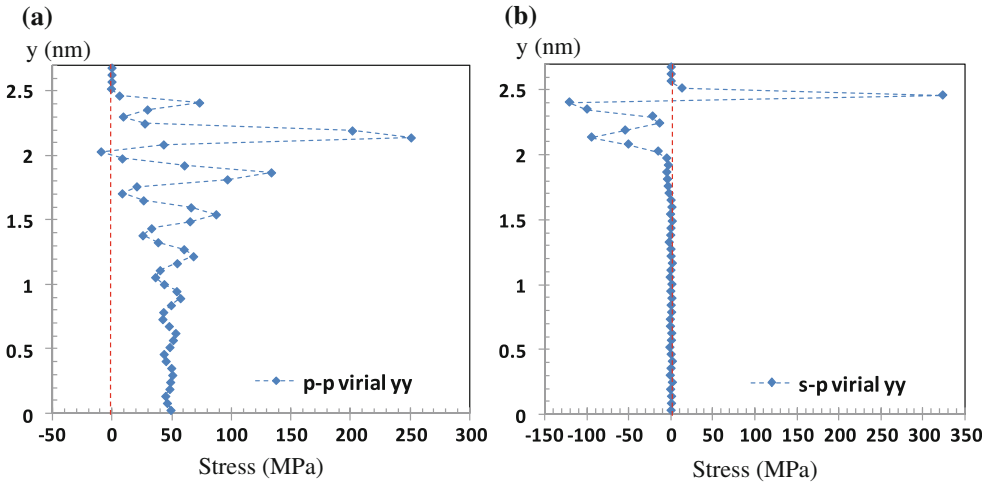

Fig. 12 Variation of the *yy* component of the particle–particle (**a**) and surface–particle (**b**) virial terms within half of the nanochannel for the liquid case

cannot represent the potential distribution inside the channel anymore. Variations of the particle–particle and surface–particle virial terms in the near-wall region are affected by the density profile. In Fig. 13, the fluid density is normalized using the averaged density at which the mean molecular spacing is equal to 0.366 nm. Ratio of this value to the distance where the L–J force switches sign (0.3822 nm) is 0.96. We included a *horizontal dashed line* to the normalized density profile in Fig. 13 to indicate the density values below which the intermolecular force between the two atoms become weakly attractive. Local density fluctuations in Fig. 13 can be correlated with variations in the particle–particle virial terms. When the local (normalized) density is reduced less than 0.96, the local particle–particle virial tends to decrease. The surface–particle virial exhibits two negative-peak points within $0.3\ \text{nm} < y < 0.7\ \text{nm}$ because of the locally attractive forces between the two near-surface density layers and solid. Closer to the wall, the net force induced by wall molecules on the fluid becomes repulsive, and hence, the surface–particle virial suddenly switches sign and becomes positive.

5 Conclusions

Prediction of stresses using the Irving–Kirkwood method can be greatly affected by long-range force field interactions between the molecules. Using various cut-off distances, we calculated the normal stresses (pressure) for argon gas and liquid within periodic domains and verified the results using published thermodynamic states. Regardless of the fluid's state, kinetic parts of the normal stresses capture the ideal-gas law, whereas corrections to pressure are induced by the virial components. Within a periodic domain, free of solid boundaries, fluid molecules experience particle–particle virial effects. If the force field induced by the mean molecular spacing at a given density is attractive, the particle–particle virial becomes negative. The virial terms become positive for molecular separations (i.e., densities) that lead to repulsion. We have observed that using 1.08-nm cut-off distance in L–J force calculations can induce significant errors in prediction of the thermodynamic state for dense gas and liquids. However, use of 2.7-nm cut-off distance resulted in reliable pressure predictions, despite the 244-fold increase ($\approx 2.5^6$) in the

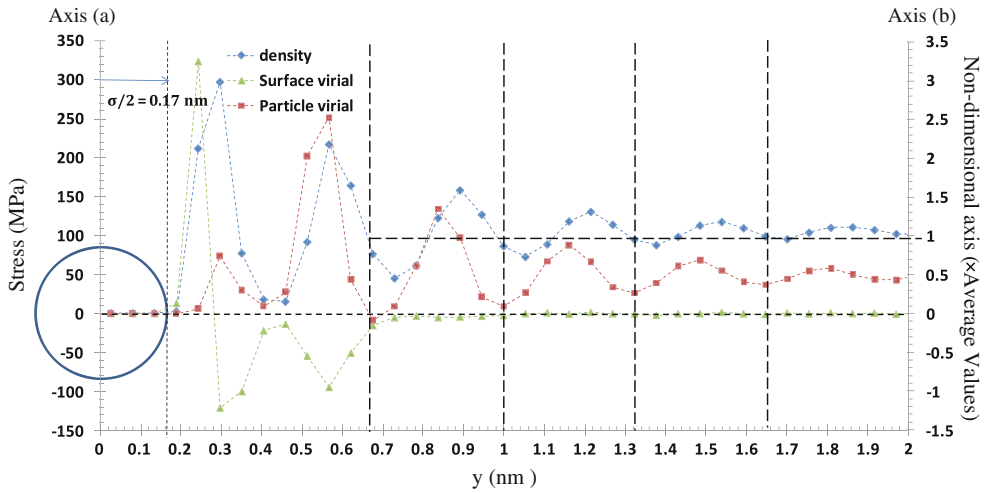

Fig. 13 Variation of the *yy* component of the surface–particle and particle–particle virial terms (*Axis a*) and the normalized density (×20.35 #/nm^3) distribution (*Axis b*) near the wall

computational cost. Neglection of the weakly attractive interaction forces because of the use of small cut-off distances in MD results in overprediction of the local pressure, which is a numerical artifact relevant to the virial calculations only.

Density buildup with a single peak is observed for the dilute gas confined within a nanochannel. The normal stresses are anisotropic within the force field penetration region, which extends approximately 1.08 nm from each wall. Beyond this distance, the ideal-gas law is valid and the density is uniform in the channel. Simulations performed at different gas/wall interaction strength ratios (ε_{wf}) show more distinct density buildup near the wall with almost linear increase in the magnitude of the surface–particle virial effects. Dense gas case exhibited onset of density-layering effects. Anisotropic normal stresses are observed approximately 1.2 nm from each wall. Beyond this distance, pressure reached its thermodynamic value. The liquid case shows well-known density-layering effects with anisotropic normal stresses penetrating more than 2 nm from each wall. In the bulk of the channel, thermodynamic pressure is reached. In addition to the kinetic part of the normal stress tensor being isotropic and able to recover the ideal-gas law, our observations show that:

(1) Wall-force field induces anisotropic normal stresses on the fluid by the surface–particle virial terms, which becomes zero beyond the wall-force field penetration depth.
(2) An additional wall effect is because of the density layering induced by the wall-force field, where the particle–particle virial terms induce further anisotropy that protrudes beyond the wall-force penetration distance. This effect becomes more dominant in liquids as a result of strong density layering.

Because of the anisotropic normal stress distribution, it is impossible to define pressure in the near-wall region of nanoscale-confined fluids. We expect these observations to be valid for flow cases, which will be presented in future studies.

Acknowledgments This work was supported by the National Science Foundation under Grant No. DMS 0807983.

References

Allen MP, Tildesley DJ (1989) Computer simulation of liquids. Oxford Science Publications Oxford University Press, New York
Barisik M, Kim B, Beskok A (2010) Molecular dynamics simulations of nanoscale gas flows. Commun Comput Phys 7:977–993
Cercignani C, Lampis M (1971) Kinetic models for gas-surface interactions. Transport Theory Stat Phys 1:101–114
Cercignani C, Pagani CD (1966) Variational approach to boundary value problems in kinetic theory. Phys Fluids 9:1167–1173
Cieplak M, Koplik J, Banavar JR (1999) Applications of statistical mechanics in subcontinuum fluid dynamics. Phys Stat Mech Appl 274(1–2):281–293
Cieplak M, Koplik J, Banavar JR (2001) Boundary conditions at a fluid-solid interface. Phys Rev Lett 86(5):803–806
Evans DJ, Hoover WG (1986) Flows far from equilibrium via molecular-dynamics. Annu Rev Fluid Mech 18:243–264
Frenkel D, Smit B (2002) Understanding molecular simulation: from algorithms to applications. Elsevier, San Diego
Guo M, Lu BCY (1997) Long range corrections to thermodynamic properties of inhomogeneous systems with planar interfaces. J Chem Phys 106(9):3688–3695
Irving JH, Kirkwood JG (1950) The statistical mechanical theory of transport processes. IV. The equations of hydrodynamics. J Chem Phys 18:817–829
Karniadakis GE, Beskok A, Aluru N (2005) Micro flows and nano flows: fundamentals and simulation. Springer-Verlag, New York
Kim BH, Beskok A, Cagin T (2008a) Thermal interactions in nanoscale fluid flow: molecular dynamics simulations with solid–liquid interfaces. Microfluid Nanofluid 5(4):551–559

Kim BH, Beskok A, Cagin T (2008b) Molecular dynamics simulations of thermal resistance at the liquid–solid interface. J Chem Phys 129:174701

Kim BH, Beskok A, Cagin T (2010) Viscous heating in nanoscale shear driven liquid flows. Microfluid Nanofluid 9:31–40

Lee J, Aluru NR (2010) Separation of gases from gas–water mixtures using carbon nanotubes. Appl Phys Lett 96:133108

Li Y, Xu J, Li D (2010) Molecular dynamics simulation of nanoscale liquid flows. Microfluid Nanofluid. doi:10.1007/s10404-010-0612-5

Mecke M, Winkelman J, Fischer J (1997) Molecular dynamic simulation of the liquid–vapor interface: the Lennard–Jones fluid. J Chem Phys 107(21):9264–9270

Sonntag RE, Borgnakke C (2002) Tables of thermodynamics and transport properties: computer-aided thermodynamic tables software provided by fundamentals of thermodynamics. Wiley, New York

Steele WA (1973) The physical interaction of gases with crystalline solids I. Gas-solid energies and properties of isolated adsorbed atoms. Surf Sci 36:317–352

Thompson PA, Troian SM (1997) A general boundary condition for liquid flow at solid surfaces. Nature 389(6649):360–362

Toth J (2002) Adsorption: theory modeling and analysis. Marcel Dekker, New York

Tsai DH (1971) The virial theorem and stress calculation in molecular dynamics. J Chem Phys 70(3):1375–1382

Zhou L (2007) Adsorption: progress in fundamental and application research. World Scientific, New York